ACS OMEGA

Open Access

http://pubs.acs.org/journal/acsodf

Article

Understanding the Reversible Transition of Unipolar and Bipolar Resistive Switching Characteristics in Solution-Derived Nanocrystalline Au−Co_3O_4 Thin-Film Memristors

Chuangye Yao,[‖] Jiacheng Li,[‖] Hongqiao Zhang, and Tao Tian*

Cite This: *ACS Omega* 2024, 9, 33941−33948

Read Online

ACCESS | Metrics & More | Article Recommendations | Supporting Information

ABSTRACT: Nanocrystalline Au−Co_3O_4 thin films were fabricated through a facile solution-processing method, and voltage-polarity-dependent resistive switching (RS) characteristics including variability of Set/Reset voltages, stability of cycling endurance, and carriers transport mechanism were studied in the Pt/Au−Co_3O_4/Pt memory devices. The switching voltages of the Set and Reset processes in the bipolar RS memristors exhibited lower variability as compared to the unipolar resistance switching devices. Moreover, the switching performance of cycle-to-cycle endurance in bipolar mode had a smaller fluctuation than those of unipolar switching behavior. Based on the current−voltage curve fitting analysis, it was found that Ohmic-conduction behaviors dominated the carriers transport of low-resistance state regardless of unipolar or bipolar switching behaviors. The carrier transport of high resistance state was governed following Poole−Frenkel emission and Schottky emission mechanisms in the unipolar and bipolar switching modes, respectively. The physical switching mechanism of Pt/Au−Co_3O_4/Pt memory devices was proposed using the model by means of growth and disruption of conducting filaments, involved in memory effects of thermochemical mechanism and valence change mechanism in the unipolar and bipolar RS, respectively. The proposed model following the finite element method revealed the roles of electrical field distribution and temperature gradient to further clarify the RS mechanism. Our results open a door for understanding and optimizing oxide-based thin-film resistance switching memory devices.

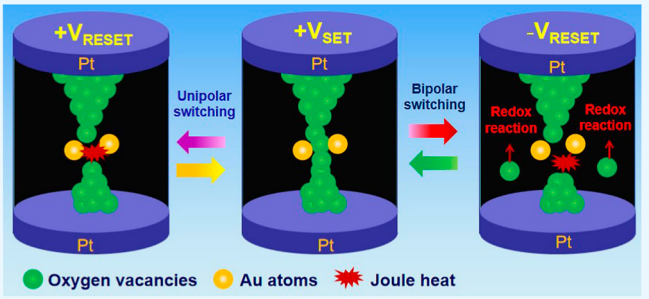

1. INTRODUCTION

The innovation of the modern electronics and information industries relies on high-performance storage technology. Memristors based on the resistive-switching effect have triggered enormous concerns due to their potential applications in artificial intelligence (AI), neuromorphic-computing simulation, and logic-operation circuit.[1−4] Professor Chua predicated theoretically the existence of memristors in 1971, and Hewlett-Packard laboratories implemented a physical prototype of the memristors with a sandwich structure until 2008.[5] In the time that follows, memristive technologies mainly focus on resistive switching (RS) materials, physical RS mechanisms, and advanced applications such as AI and neuromorphic-computing simulation.[1] Cao et al. reported that memristor-based neural networks were used for the preparation of different AI systems.[1] Wang et al. fabricated a flexible $HfAlO_x$-based memristor, suggesting that their memristor is capable of simulating brain-inspired neuromorphic computing behaviors, such as long-term plasticity and long-term depression.[6] The memristors for memory applications are called resistive random access memory (RRAM).[7] RRAM devices with a sandwich-based structure are considered as a future promising competitor due to their unique advantages such as low-power consumption, fast speed of reading/writing process, and compatibility with the semiconductor fabrication process.[8,9]

RS effect can be classified into two types, unipolar and bipolar switching behaviors, based on the characteristics of voltage polarity.[10] The unipolar switching behavior exhibits the demand of resistance switching on the external voltage polarity, where Set or Reset operation changes occur on the same polarity of the bias voltage applied to the electrode. Similarly, during the bipolar switching process, the process of Set and Reset changes occurs in opposite polarity of the external voltage. Among them, a unipolar switching device allows a diode as the selector in crossbar arrays to settle the sneak-path issue, and one diode-one resistor structure owns advantages in achieving the higher integration density for large-scale integrated circuit applications.[11] Bipolar switching devices

Received: May 9, 2024
Revised: July 5, 2024
Accepted: July 9, 2024
Published: July 23, 2024

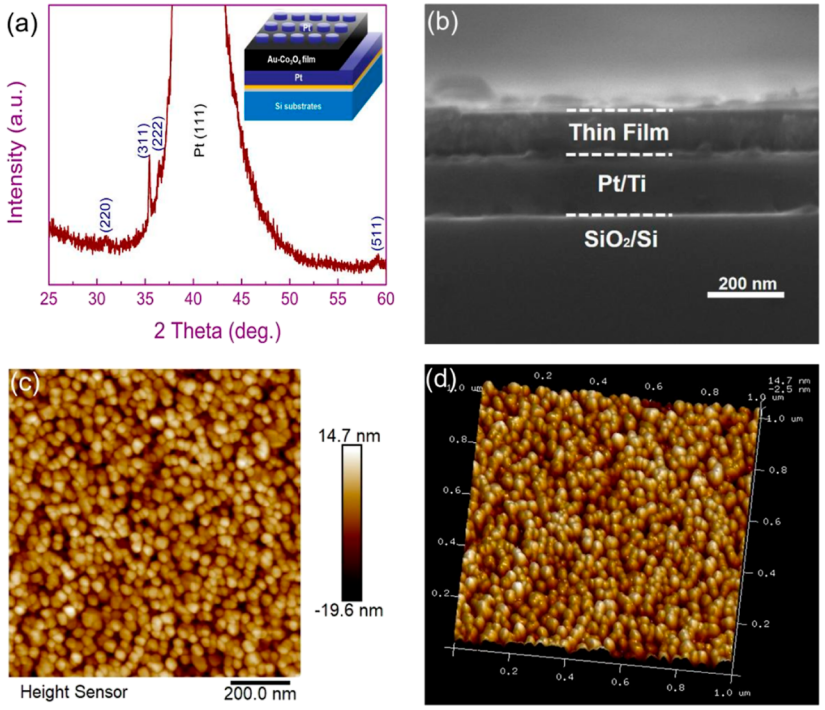

Figure 1. (a) XRD pattern of a Au−Co_3O_4 thin film memory device. The inset displays the schematic diagram of Pt/Au−Co_3O_4/Pt structures. (b) Cross-sectional SEM image of Au−Co_3O_4 thin films grown on the Pt/Ti/SiO_2/Si substrate. (c) AFM image of Au−Co_3O_4 thin films. (d) Corresponding three-dimensional surface AFM image of Au−Co_3O_4 thin films.

can acquire faster switching speed, lower operation consumption, and better uniformity/stability as compared to unipolar switching device.[11] In previous research, unipolar and bipolar switching behaviors are usually presented in different devices, explained by different mechanisms, such as unipolar switching according to thermochemical mechanism and bipolar switching corresponding to electrochemical metallization or valence-change mechanism.[12] It may limit the development of RS device miniaturization to some extent, especially for the fabrication of memory devices with both unipolar and bipolar functions. Integration of unipolar and bipolar functions into a single RS device will greatly increase the integration density for the realization of high-performance information storage. Therefore, it is very important to develop a unipolar-bipolar integrated memory device and understand the reversible transition between unipolar and bipolar RS behaviors. Furthermore, the above research situation motivated us to explore the reversible switching mechanisms of unipolar and bipolar RS behaviors. Over the past decade, the investigation on RS mechanisms has hold dispute. At present, the most widely accepted theory is the conducting filament model where the random growth and disruption of conducting filaments bring about the dispersed RS parameters.[13,14] Therefore, a deeper understanding of the RS mechanism is still crucial for enhancing the reliability and stability of the RRAM device.

From the perspective of exploring RS materials, lots of materials have shown RS performance.[15,16] However, metal oxides are more favored owing to their stable physical/chemical characteristics, simple preparation, and compatibility with magnetic/optical properties.[17,18] Recently, spinel materials have exhibited excellent RS characteristics, such as spinel-structured oxides: $NiFe_2O_4$, $CoFe_2O_4$, $ZnFe_2O_4$, $MnCo_2O_4$, and Co_3O_4,[19−25] which suggested that the spinel structure of materials owns superiority for RS application. Among them, spinel-structure Co_3O_4 is an outstanding candidate for RRAM device applications because of the simple binary compositions, friendly compatibility with magnetism, adjustable valence conversion, and good p-type semiconductor properties.[25,26] To date, there are relatively few studies of the RS properties of spinel cobalt oxide (Co_3O_4). Our previous research work confirmed that introducing Au nanoparticles into Co_3O_4 thin films can improve bipolar RS parameters of Co_3O_4 thin film devices, based on that Au nanoparticles can create an enhancement of the local electric field.[25] In such a point of view, it is speculated that the Au−Co_3O_4 composite thin film is desirable for RS memory device application. However, until very recently, there is no report for unipolar RS properties of Au−Co_3O_4 nanocomposite device, and coexistence of unipolar and bipolar switching characteristics as well as their reversible-switching mechanism in a single memory cell based on spinel Au−Co_3O_4 nanocomposite thin films has not been reported yet.

In this study, nanocrystalline Au−Co_3O_4 thin films with spinel structures were fabricated on Pt/Ti/SiO_2/Si substrates by using a facile solution-processing method owing to the advantages such as high versatility, stable chemical homogeneity, low cost, and a simple fabrication of two-terminal structures.[12] Coexistence of unipolar and bipolar switching behaviors was achieved in a single Pt/Au−Co_3O_4/Pt memory device. The surface and cross-sectional morphologies of thin films, voltage-polarity-dependent RS characteristics, and carrier transport mechanism were explored. In addition, the differences of the RS mechanism between unipolar and bipolar switching were clarified in terms of a physical model of conductive filaments and oxygen vacancies.

https://doi.org/10.1021/acsomega.4c04429
ACS Omega 2024, 9, 33941−33948

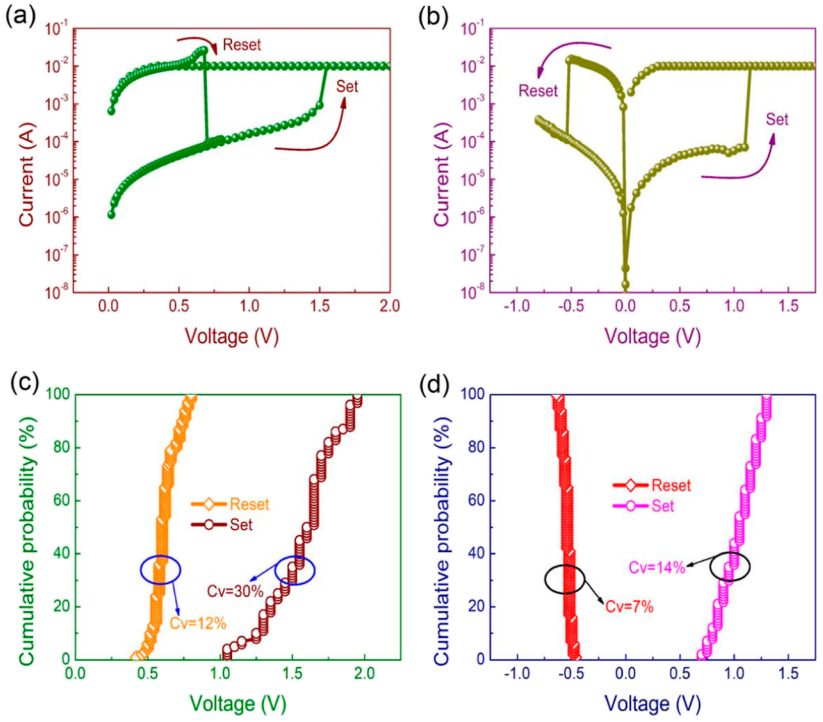

Figure 2. Typical $I-V$ characteristics of (a) unipolar and (b) bipolar RS of Pt/Au−Co_3O_4/Pt devices. Statistical distribution of the Set and Reset voltages of Pt/Au−Co_3O_4/Pt devices following (c) unipolar and (d) bipolar RS.

2. MATERIALS AND METHODS

2.1. Fabrication of Thin Films and Devices. Nanocrystalline Au−Co_3O_4 films were synthesized onto a Pt/Ti/SiO_2/Si substrate by using a low-cost solution-processing method. The details for preparing spinel Au−Co_3O_4 thin film-based RRAM devices were reported in our previous research,[25] in which an appropriate Au concentration of 0.75% was verified for RS enhancement. Accordingly, the amount of Au additive obeyed the molar ratio of Au to Co_3O_4 of 0.75%:1 for preparation of the precursor solution. The synthesized-precursor solution was spin-coated onto the surface of the Pt/Ti/SiO_2/Si substrate (bottom Pt electrode) at 3000 rpm for 30 s and then baked at 300 °C for 5 min to eliminate the residual organic matter. The operation of spin-coating and baking was repeatedly carried out until acquiring the needed film thickness. To improve compactness and crystallization of thin films, the resultant thin films were thermally annealed at 600 °C for 1 h. After that a top electrode of platinum (Pt) was deposited on the surface of the Au−Co_3O_4/Pt/Ti/SiO_2/Si stacked structure by means of a direct-current sputtering method.

2.2. Material Characterizations and Measurements. The crystal structure of the spinel Au−Co_3O_4 thin films was inspected by using the X-ray diffraction (XRD) technology with a Rigaku D/Max-2400 diffractometer. Field emission scanning electron microscopy (SEM, Gemini 500) was used to observe the cross-sectional morphologies and film thickness of the Au−Co_3O_4 thin films. The surface and three-dimensional morphologies of the Au−Co_3O_4 thin films were obtained by using Bruker-type atomic force microscopy (AFM). The RS parameters of the Pt/Au−Co_3O_4/Pt stacked devices were investigated by using a Keithley 236 sourcemeter, and temperature-dependent current−voltage ($I-V$) curves were measured from 200 to 300 K. The finite element method with COMSOL Multiphysics 5.4 was used to simulate the electric field and temperature gradient distribution during the RS process.

3. RESULTS AND DISCUSSION

The crystallinity of the Au−Co_3O_4 thin films and Pt electrode layer were examined by the XRD characterization, as shown in Figure 1a, in which the inset shows the Pt/Au−Co_3O_4/Pt stacked structure. The XRD pattern indicated that the diffraction peaks of (220), (311), (222), and (511) are in accordance with the cubic spinel lattice of the composite films, confirming a single phase without impurity.[25] Figure 1b illustrates the cross-sectional SEM image of Au−Co_3O_4 thin films grown on Pt/Ti/SiO_2/Si substrates. As can be observed, the thickness of the thin films acting as an active layer for RS is around 120 nm. Furthermore, AFM characterization was used to observe the surface morphologies of Au−Co_3O_4 thin films, as shown in Figure 1c,d. The root-mean-square roughness is 5.11 nm, and the average roughness is 4.09 nm, demonstrating that the surface of the solution-derived Au−Co_3O_4 thin films is smooth and compact. Based on AFM characterization, the average size of surface particle is about 27 nm in view of the profile confirmation, demonstrating the nanocrystalline nature in our synthesized composite thin films.

Typical $I-V$ characteristics of the Au−Co_3O_4 thin-film RS devices are plotted after an electroforming process, as shown in Figure 2a,b. It can be observed from Figure 2a that a positive Set operation switches device from high-resistance state (HRS) to low-resistance state (LRS) owing to the formation of conductive filaments, and the device is switched by a positive Reset operation from LRS to HRS due to the disruption of conducting filaments.[27] This behavior is well matched to unipolar RS that can be activated by the external bias voltage at the same polarity. On the contrary, bipolar RS can be activated by the external bias voltage at the opposite polarity such as

https://doi.org/10.1021/acsomega.4c04429
ACS Omega 2024, 9, 33941−33948

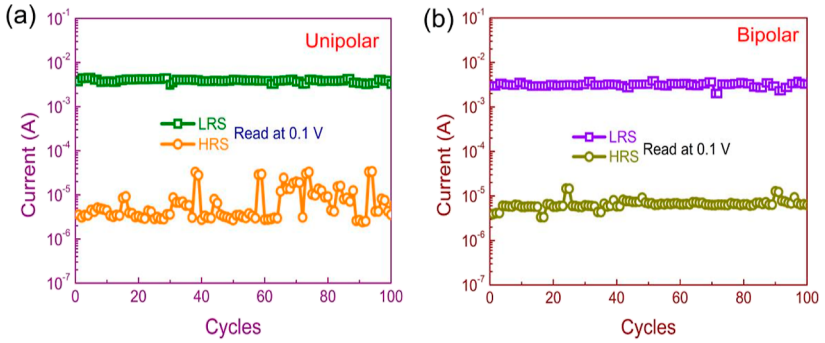

Figure 3. Cycle-to-cycle endurance characteristics of Pt/Au−Co_3O_4/Pt devices following (a) unipolar and (b) bipolar RS.

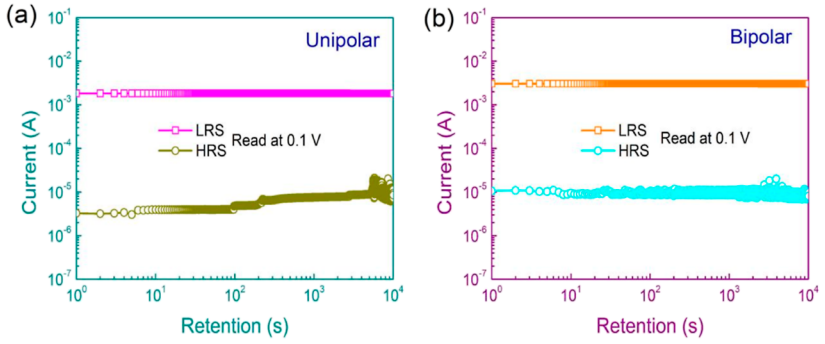

Figure 4. Retention characteristics of Au−Co_3O_4 thin film memory devices following (a) unipolar and (b) bipolar RS.

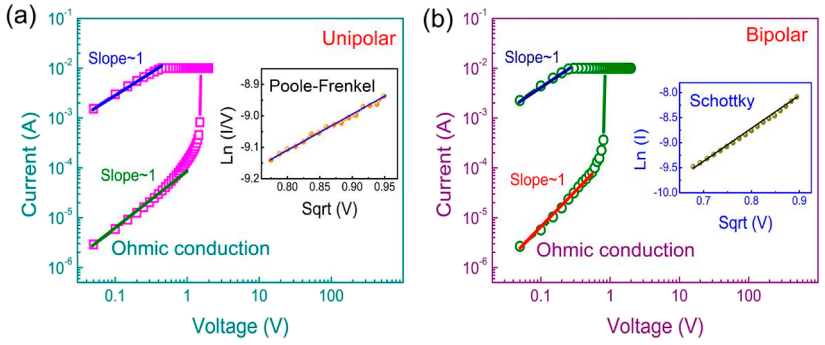

Figure 5. (a) Double-log scale $I-V$ curves of unipolar RS of Pt/Au−Co_3O_4/Pt devices. The inset shows the typical Ln (I/V) versus Sqrt (V) plot of HRS under the unipolar RS mode. (b) Double-log-scale $I-V$ curves of bipolar RS of Pt/Au−Co_3O_4/Pt devices. The inset shows the typical Ln (I) versus Sqrt (V) plot of HRS under the bipolar RS mode.

positive Set process and negative Reset process, as shown in Figure 2b. To further distinguish electrical characteristics of unipolar and bipolar RS devices, Figure 2c,d shows the Set/Reset voltage distribution of 100 consecutive unipolar and bipolar RS, respectively. The switching voltage uniformity of the Set/Reset process can be evaluated by using a coefficient of variation (Cv) as follows[28]

$$\mathrm{Cv} = \frac{\delta}{\mu} \times 100\% \tag{1}$$

where δ and μ denote the standard deviation and absolute mean value, respectively. As shown in Figure 2c,d, compared with the unipolar switching behavior, the bipolar switching of the Au−Co_3O_4 thin-film RS devices exhibits lower Cv values of the Set voltages from 30 to 14% and Reset voltages from 12 to 7%, which suggested that bipolar RS owns more uniform switching voltages in the Au−Co_3O_4 thin film memory devices. The improved uniformity of switching voltages may be related to the variations of defect concentration such as oxygen vacancies.[25,29]

Figure 3 shows cycle-to-cycle endurance characteristics of Au−Co_3O_4 thin film memristors following unipolar and bipolar RS. The resistance ratios (R_{OFF}/R_{ON}) > 10 were observed, regardless of unipolar switching from Figure 3a or bipolar RS from Figure 3b, which meets the requirements for applications of RS memories.[12] In addition, both of the switching modes exhibited the identical resistance levels of HRS and LRS. However, it can be found that the cycle-to-cycle endurance performance at HRS of unipolar switching showed an obvious fluctuation as compared to that of bipolar RS, which may be attributed to random formation and rupture of conducting filaments.[30] The above results suggested that bipolar RS exhibited better RS properties.

As can be seen in Figure 4, the current at HRS of unipolar switching increased obviously as the retention time increased, and the current at HRS of bipolar switching decreased a little,

https://doi.org/10.1021/acsomega.4c04429
ACS Omega 2024, 9, 33941−33948

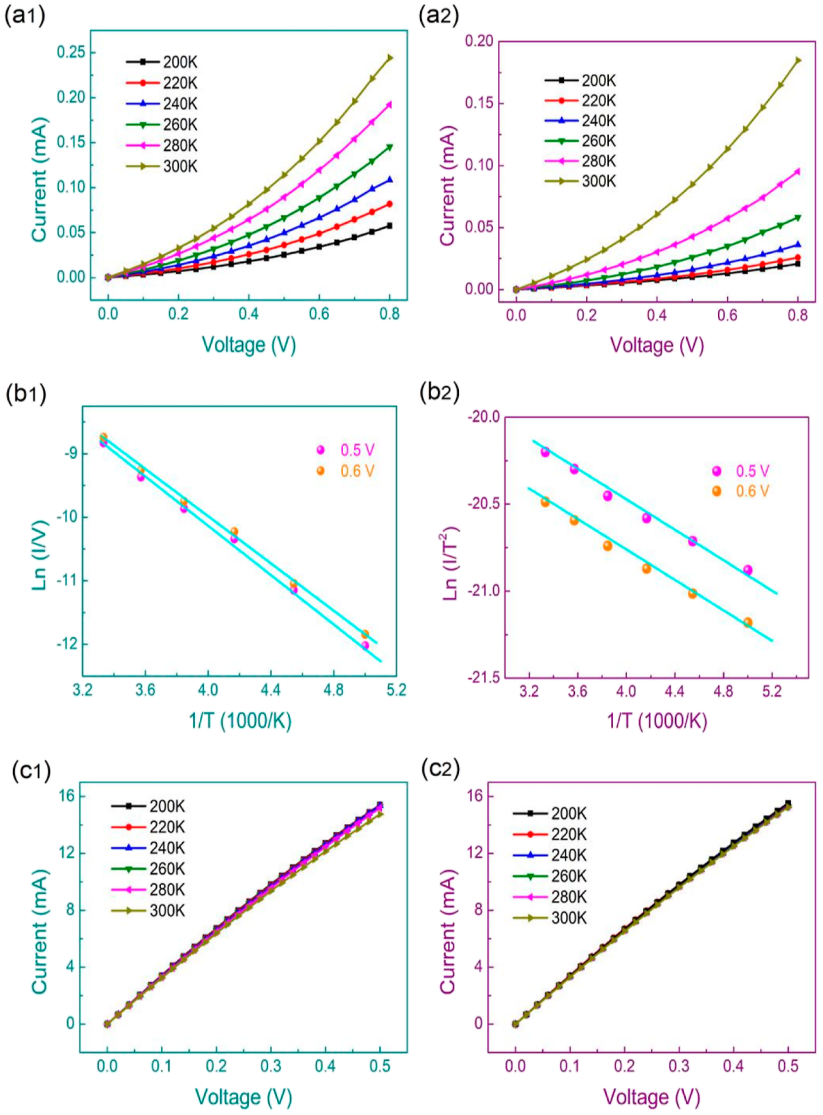

Figure 6. Temperature dependence of $I-V$ curves of the Au−Co_3O_4 based device at HRS following (a1) unipolar and (a2) bipolar RS. (b1) Ln (I/V) versus $1/T$ plot and (b2) Ln (I/T^2) versus $1/T$ plot for HRS of the Au−Co_3O_4 based device recorded from 0.5 to 0.6 V. Temperature dependence of $I-V$ curves of the Au−Co_3O_4 based device at LRS following (c1) unipolar and (c2) bipolar RS.

but the ratio between HRS and LRS was still higher than 100. The current at HRS of unipolar switching device exhibited a large fluctuation after the retention time is over 5×10^3 s. Compared with the unipolar switching device, no obvious degradation over 10^4 s for the bipolar switching device suggested a good retention performance, and it also confirmed the nonvolatile nature of the RS device.

The carrier transport mechanisms were investigated based on the fitting analysis of $I-V$ curves, as shown in Figure 5. Figure 5a shows the double-log scale $I-V$ curves of unipolar RS of Au−Co_3O_4 thin film memory devices during the Set process, and the fitting of $I-V$ curve at LRS is linear with slope ∼1, suggesting an Ohmic conduction behavior and filament formation. The $I-V$ fitting curve at the low-voltage region of HRS is also linear with slope ∼1 and Ohmic conduction mechanism, which can be attributed to that the injected carrier concentrations are lower than the equilibrium-carrier concentration.[29] However, the $I-V$ fitting curve at the higher voltage region of HRS is nonlinear, which can be fitted by the linear relation of Ln (I/V) versus Sqrt (V), as shown in the inset of Figure 5a, in accordance with the Poole−Frenkel emission mechanism. Similarly, the $I-V$ fitting curve of bipolar RS at LRS and low-voltage region of HRS is linear (slope ∼1) and obeys Ohmic conduction behavior, as shown in Figure 5b, while the high-voltage region of HRS can be fitted by the linear relation of Ln (I) versus Sqrt (V), as shown in the inset of Figure 5b, indicating the Schottky emission mechanism. The fitted results of $I-V$ curves at HRS of unipolar and bipolar RS followed different carrier transport mechanisms, which may be due to that the concentrations of trap or defects exhibited variation via the combined roles of electrical field effect and Joule-heating effect.[31]

As can be seen from Figure 6a1,a2, the measured temperature increased from 200 to 300 K at HRS of the Au−Co_3O_4 based device, and the values of current increased, which suggested that the resistances decreased with increasing temperature regardless of unipolar or bipolar RS, corresponding to semiconductor characteristics. For the unipolar RS, the plot of Ln (I/V) versus $1/T$ at HRS of the Au−Co_3O_4 based device recorded from 0.5 to 0.6 V is displayed in Figure 6b1.

https://doi.org/10.1021/acsomega.4c04429
ACS Omega 2024, 9, 33941−33948

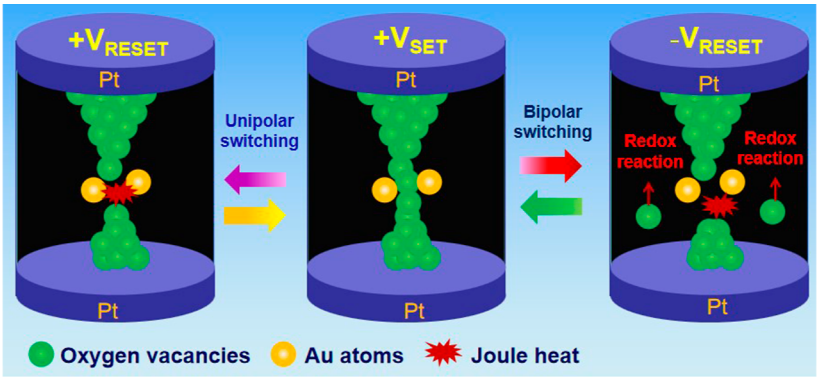

Figure 7. Schematic diagrams showing the RS mechanism of Pt/Au−Co_3O_4/Pt devices following different voltage polarities.

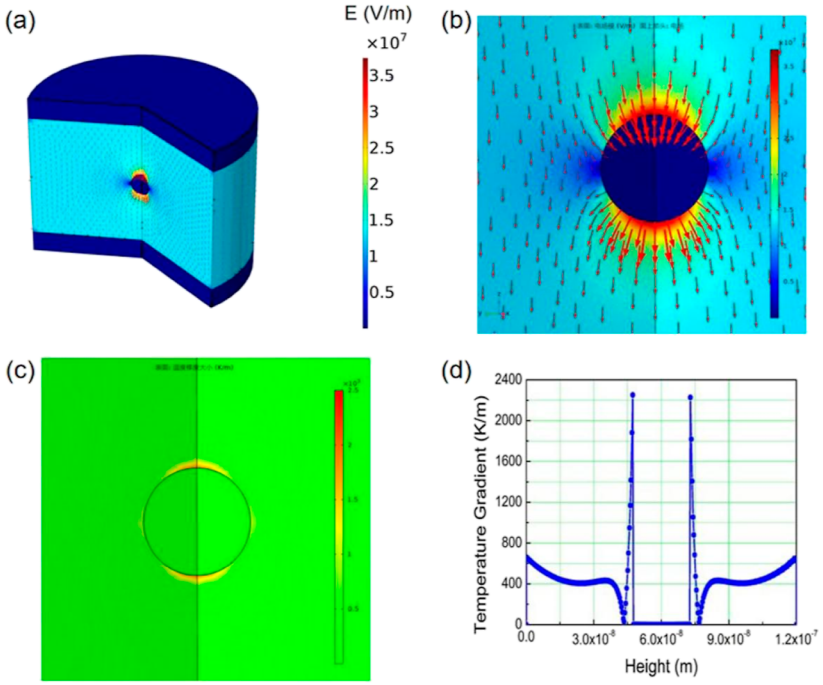

Figure 8. (a) Three-dimensional and (b) two-dimensional images of the electric field distribution of the Pt/Au−Co_3O_4/Pt RS device. (c) Thermal field simulation of the Pt/Au−Co_3O_4/Pt RS device. (d) Variation of temperature gradient of the Pt/Au−Co_3O_4/Pt RS device.

The plot from 0.5 to 0.6 V is nearly straight line, which suggested that the conduction mechanism of HRS for unipolar RS was governed by Poole−Frenkel emission.[32] For the bipolar RS, Figure 6b2 depicts Ln (I/T^2) versus $1/T$ plot for HRS of the Au−Co_3O_4 based device recorded from 0.5 to 0.6 V. The Ln (I/T^2) versus $1/T$ plot is nearly straight line, which confirmed that the conduction mechanism of HRS for bipolar RS was in accordance with Schottky emission.[31] As shown in Figure 6c1,c2, as the measured temperature increased, the values of current decreased, and the resistances increased at LRS of the Au−Co_3O_4 based device regardless of unipolar or bipolar RS, suggesting metal-like behaviors and formation of conductive filament at LRS of the RS process.

Based on the above discussion, the transition of unipolar and bipolar switching in the Au−Co_3O_4 thin film-based devices can be schematically illustrated by means of the model of growth and rupture of oxygen vacancy-based conductive filaments,[25,27,29] as shown in Figure 7. During the positive Set process, the local filamentary conduction paths formed in the switching layer of thin films and the device switches from HRS to LRS. That is, the oxygen ions motion because of transition with oxygen coordination from lattice results in formation and accumulation of multiple oxygen vacancies, and the local filamentary conduction paths composed of oxygen vacancies are then created in the switching thin films between the top and bottom electrodes.[30] Meanwhile, Au nanoparticles can assist in the formation of confined oxygen vacancy-based conducting filaments due to the enhancement of the local electric-field effect which can guide the filament growth. Following that (i) during the positive Reset $(+V_{Reset})$ process of unipolar switching behavior, the device recovered to HRS due to the Joule-heating effect derived rupture of oxygen vacancy-based conductive filament,[33] and thus fused out the weak part of the filaments.[34] Although the local filamentary path ruptured under the Reset switching process, some defects such as oxygen vacancies and residue filament remained in the films.[35] The Joule-heating dominated unipolar RS behavior based on current-induced increase of the temperature can be ascribed to the thermochemical memory effect.[12] (ii) During the negative Reset $(-V_{Reset})$ process of bipolar switching

https://doi.org/10.1021/acsomega.4c04429
ACS Omega 2024, 9, 33941−33948

behavior, the device turns back to HRS because oxygen vacancies acquire transition to oxygen ions via redox reaction following a negative voltage, as well as existence of the Joule-heating effect due to the increase of temperature. The voltage polarity-dominated bipolar RS behavior is in conformity with the valence change memory effect because of the generation or annihilation of oxygen vacancies, associated with the oxygen-ion motion due to the electrical field effect.[12] Therefore, the reversible transition of unipolar and bipolar RS behaviors between HRS and LRS was realized following the formation and rupture of oxygen vacancy-based conductive filaments.

The bipolar RS characteristics of the Au−Co_3O_4 thin film device exhibited a more stable performance of RS. To obtain better understanding of the bipolar RS mechanism in the Au−Co_3O_4 thin film device, we carried out a finite element simulation by using COMSOL Multiphysics. The simulation geometry is composed of two platinum electrode layers and the composite Au−Co_3O_4 active layer, as shown in Figure 8a. The needed parameters of the simulation process are mainly the material properties, as similar to a previous research work.[36] In this simulation, Supporting Information Table S1 displays the material parameters related to the COMSOL simulation. The electric field distribution of the Pt/Au−Co_3O_4/Pt device during the Set process is shown in Figure 8a,b, an enhancement of local electric field was observed near Au nanoparticles, and the conductive filament prefers formation along the direction of the local electric field. As shown in Figure 8c,d, the temperature gradient distribution of the Pt/Au−Co_3O_4/Pt device indicated that a maximum value occurred near Au nanoparticles, reaching 2200 K/m, while the edge of Au nanoparticles was lower than 800 K/m. The local distortion of the electric-field and temperature-field effect can induce that oxygen vacancies prefer to concentrate near Au nanoparticles, which results in the formation and disruption of confined oxygen vacancy-based conductive filaments, further-ing reducing randomness of conductive filament growth and improving RS parameters.

4. CONCLUSIONS

In summary, a Pt/Au−Co_3O_4/Pt sandwich structure device fabricated via a low-cost solution-processing method was examined for its RS characteristics in RRAM applications. *I*−*V* measurements confirmed the coexistence of unipolar and bipolar RS behaviors. Statistical analysis of switching voltages suggested that the coefficients of variation of Reset and Set voltages are only 7 and 14%, respectively, revealing better uniformity in bipolar switching behavior. More stable cycle-to-cycle endurance performance was achieved in the bipolar RS behavior of Au−Co_3O_4 thin-film devices. The conduction mechanisms involve Ohmic conduction (dominant at LRS), Poole−Frenkel conduction (dominant at HRS of the unipolar mode), and Schottky conduction (dominant at HRS of the bipolar mode). The switching mechanism was attributed to the formation and disruption of oxygen vacancy-based conductive filaments.

■ ASSOCIATED CONTENT

Supporting Information

The Supporting Information is available free of charge at https://pubs.acs.org/doi/10.1021/acsomega.4c04429.

Material parameters related to COMSOL simulation (PDF)

■ AUTHOR INFORMATION

Corresponding Author

Tao Tian − *Hunan Provincial Key Laboratory of Xiangnan Rare-Precious Metals Compounds Research and Application, School of Chemistry and Environmental Science, Xiangnan University, Chenzhou 423000, China*; Email: taotian@xnu.edu.cn

Authors

Chuangye Yao − *Microelectronics and Optoelectronics Technology Key Laboratory of Hunan Higher Education, School of Physics and Electronic Electrical Engineering, Xiangnan University, Chenzhou 423000, China*; orcid.org/0009-0002-8456-9378

Jiacheng Li − *Guangxi Academy of Sciences, Nanning 530007, China*

Hongqiao Zhang − *Microelectronics and Optoelectronics Technology Key Laboratory of Hunan Higher Education, School of Physics and Electronic Electrical Engineering, Xiangnan University, Chenzhou 423000, China*

Complete contact information is available at: https://pubs.acs.org/10.1021/acsomega.4c04429

Author Contributions

‖C.Y. and J.L. contributed equally to this work.

Notes

The authors declare no competing financial interest.

■ ACKNOWLEDGMENTS

The authors gratefully acknowledge financial supports from the Hunan Provincial Natural Science Foundation of China (nos. 2022JJ40414 and 2024JJ7512), the Research Foundation of the Department of Natural Resources of Hunan Province, China (no. 20230140ST), the Scientific Research Fund of Hunan Provincial Education Department (nos. 21C0725 and 23B0782), the Applied Characteristic Discipline of Electronic Science and Technology of Xiangnan University (no. XNXY20221210), the College students' Innovation and Entrepreneurship Training Program of Xiangnan University (nos. X2023050 and X2023054), and the Scientific Research Program of Xiangnan University (nos. 2021XJ36 and 2023XJ05).

■ REFERENCES

(1) Cao, Z.; Sun, B.; Zhou, G.; Mao, S.; Zhu, S.; Zhang, J.; Ke, C.; Zhao, Y.; Shao, J. Memristor-based Neural Networks: A Bridge from Device to Artificial Intelligence. *Nanoscale Horiz.* **2023**, *8*, 716−745.

(2) Shi, T.; Wang, R.; Wu, Z.; Sun, Y.; An, J.; Liu, Q. A Review of Resistive Switching Devices: Performance Improvement, Characterization, and Applications. *Small Struct.* **2021**, *2*, 2000109.

(3) Moazzeni, A.; Riyahi Madvar, H.; Hamedi, S.; Kordrostami, Z. Fabrication of Graphene Oxide-Based Resistive Switching Memory by the Spray Pyrolysis Technique for Neuromorphic Computing. *ACS Appl. Nano Mater.* **2023**, *6*, 2236−2248.

(4) Milano, G.; Porro, S.; Valov, I.; Ricciardi, C. Recent Developments and Perspectives for Memristive Devices Based on Metal Oxide Nanowires. *Adv. Electron. Mater.* **2019**, *5*, 1800909.

(5) Mao, S.; Sun, B.; Zhou, G.; Yang, Y.; Zhao, H.; Zhou, Y.; Chen, Y.; Zhao, Y. Analog-to-Digital and Self-Rectifying Resistive Switching Behavior Based on Flower-Like δ-MnO_2. *Appl. Surf. Sci.* **2022**, *595*, 153560.

(6) Wang, T.-Y.; Meng, J.-L.; Chen, L.; Zhu, H.; Sun, Q.-Q.; Ding, S.-J.; Bao, W.-Z.; Zhang, D. W. Flexible 3D Memristor Array for

Binary Storage and Multi-States Neuromorphic Computing Applications. *InfoMat* **2020**, *3*, 212−221.
(7) Wang, C.; Shi, G.; Qiao, F.; Lin, R.; Wu, S.; Hu, Z. Research Progress in Architecture and Application of RRAM with Computing-in-Memory. *Nanoscale Adv.* **2023**, *5*, 1559−1573.
(8) Zhang, W.; Guo, Z.; Dai, Y.; Lei, J.; Wang, J.; Hu, F. Effects of Stacking Sequence and Top Electrode Configuration on Switching Behaviors in ZnO-HfO_2 Hybrid Resistive Memories. *Ceram. Int.* **2023**, *49*, 35973−35981.
(9) Bogle, K. A.; Cheng, X.; Rana, A. S.; Valanoor, N. Bi-Doped Single-Crystalline (001) Epitaxial TiO_2 Anatase Nanostructures for Resistive Random Access Memory Applications. *ACS Appl. Nano Mater.* **2020**, *3*, 1706−1712.
(10) Ismail, M.; Batool, Z.; Mahmood, K.; Manzoor Rana, A.; Yang, B.-D.; Kim, S. Resistive Switching Characteristics and Mechanism of Bilayer HfO_2/ZrO_2 Structure Deposited by Radio-Frequency Sputtering for Nonvolatile Memory. *Results Phys.* **2020**, *18*, 103275.
(11) Chen, Z.; Huang, W.; Zhao, W.; Hou, C.; Ma, C.; Liu, C.; Sun, H.; Yin, Y.; Li, X. Ultrafast Multilevel Switching in Au/YIG/n-Si RRAM. *Adv. Electron. Mater.* **2019**, *5*, 1800418.
(12) Carlos, E.; Branquinho, R.; Martins, R.; Kiazadeh, A.; Fortunato, E. Recent Progress in Solution-Based Metal Oxide Resistive Switching Devices. *Adv. Mater.* **2021**, *33*, 2004328.
(13) Zhang, Y.; Mao, G.-Q.; Zhao, X.; Li, Y.; Zhang, M.; Wu, Z.; Wu, W.; Sun, H.; Guo, Y.; Wang, L.; Zhang, X.; Liu, Q.; Lv, H.; Xue, K.-H.; Xu, G.; Miao, X.; Long, S.; Liu, M. Evolution of the Conductive Filament System in HfO_2-Based Memristors Observed by Direct Atomic-Scale Imaging. *Nat. Commun.* **2021**, *12*, 7232.
(14) Lu, Y.; Yuan, Y.; Liu, R. B.; Liu, T. Y.; Chen, J. R.; Wei, L. J.; Wu, D.; Zhang, W.; You, B.; Du, J. Improved Resistive Switching Performance and Realized Electric Control of Exchange Bias in a NiO/HfO_2 Bilayer Structure. *Phys. Chem. Chem. Phys.* **2023**, *25*, 24436−24447.
(15) Wang, H.; Yan, X. Overview of Resistive Random Access Memory (RRAM): Materials, Filament Mechanisms, Performance Optimization, and Prospects. *Phys. Status Solidi RRL* **2019**, *13*, 1900073.
(16) Wang, Z. R.; Wu, H. Q.; Burr, G. W.; Hwang, C. S.; Wang, K. L.; Xia, Q. F.; Yang, J. J. Resistive Switching Materials for Information Processing. *Nat. Rev. Mater.* **2020**, *5*, 173−195.
(17) Khot, A. C.; Desai, N. D.; Khot, K. V.; Salunkhe, M. M.; Chougule, M. A.; Bhave, T. M.; Kamat, R. K.; Musselman, K. P.; Dongale, T. D. Bipolar Resistive Switching and Memristive Properties of Hydrothermal Synthesized TiO_2 Nanorod Array: Effect of Growth Temperature. *Mater. Des.* **2018**, *151*, 37−47.
(18) Patil, A. R.; Dongale, T. D.; Kamat, R. K.; Rajpure, K. Y. Binary Metal Oxide-Based Resistive Switching Memory Devices: A Status Review. *Mater. Today Commun.* **2023**, *34*, 105356.
(19) Tong, S.-K.; Chang, J.-H.; Hao, Y.-H.; Wu, M.-R.; Wei, D.-H.; Chueh, Y.-L. Optimum Resistive Switching Characteristics of $NiFe_2O_4$ by Controlling Film Thickness. *Appl. Surf. Sci.* **2021**, *564*, 150091.
(20) Rajesh Kumar, R.; Kalaboukhov, A.; Weng, Y.-C.; Rathod, K. N.; Johansson, T.; Lindblad, A.; Kamalakar, M. V.; Sarkar, T. Vacancy Engineered Nickel Ferrite Forming-Free Low-Voltage Resistive Switches for Neuromorphic Circuits. *ACS Appl. Mater. Interfaces* **2024**, *16*, 19225−19234.
(21) Munjal, S.; Khare, N. Compliance Current Controlled Volatile and Nonvolatile Memory in Ag/$CoFe_2O_4$/Pt Resistive Switching Device. *Nanotechnology* **2021**, *32*, 185204.
(22) Rajarathinam, S.; Ganguly, U.; Venkataramani, N. Impact of Oxygen Partial Pressure on Resistive Switching Characteristics of PLD Deposited $ZnFe_2O_4$ Thin Films for RRAM Devices. *Ceram. Int.* **2022**, *48*, 7876−7884.
(23) Zhang, L.; Xie, B.; Chen, W.; Fan, L.; Zheng, H.; Wu, Q.; Zheng, P.; Zheng, L.; Zhang, Y. Resistive Switching Behaviours of Pt/$Ni_{0.5}Fe_{0.5}Zn_2O_4$/Pt Based on Film Thickness for Memristor Applications. *Ceram. Int.* **2023**, *49*, 2991−2997.
(24) Du, L.; Li, J.; Liao, Q.; Qin, N.; Bao, D. Ce-Doping at Mn Site to Enhance Resistive Switching Performance of Spinel $MnCo_2O_4$ Resistive Random Access Memory Devices. *Ceram. Int.* **2024**, *50*, 20495−20503.
(25) Yao, C.; Ismail, M.; Hao, A.; Thatikonda, S. K.; Huang, W.; Qin, N.; Bao, D. Au Nanoparticles Introduced to Spinel Co_3O_4 Thin Films: Switching Enhancement and Magnetization Modulation. *J. Magn. Magn. Mater.* **2020**, *493*, 165702.
(26) Ahn, J.; Kim, T.; Kim, Y.; Kim, E. K. Resistive Switching Behaviors of Cobalt Oxide Films with Structural Change by Post-Thermal Annealing. *Mater. Sci. Semicond. Process.* **2023**, *156*, 107295.
(27) Li, T.; Yu, H. L.; Chen, S. H. Y.; Zhou, Y.; Han, S. T. The Strategies of Filament Control for Improving the Resistive Switching Performance. *J. Mater. Chem. C* **2020**, *8*, 16295−16317.
(28) Vishwanath, S. K.; Woo, H.; Jeon, S. Enhancement of Resistive Switching Properties in Al_2O_3 Bilayer-Based Atomic Switches: Multilevel Resistive Switching. *Nanotechnology* **2018**, *29*, 235202.
(29) Yao, C. Y.; Ismail, M.; Hao, A. Z.; Thatikonda, S. K.; Huang, W. H.; Qin, N.; Bao, D. H. Annealing Atmosphere Effect on the Resistive Switching and Magnetic Properties of Spinel Co_3O_4 Thin Films Prepared by a Sol-Gel Technique. *RSC Adv.* **2019**, *9*, 12615−12625.
(30) Yao, C.; Hu, W.; Ismail, M.; Thatikonda, S. K.; Hao, A.; He, S.; Qin, N.; Huang, W.; Bao, D. Coexistence of Resistive Switching and Magnetism Modulation in Sol-Gel Derived Nanocrystalline Spinel Co_3O_4 Thin Films. *Curr. Appl. Phys.* **2019**, *19*, 1286−1295.
(31) Hu, W.; Zou, L. L.; Chen, X. M.; Qin, N.; Li, S. W.; Bao, D. H. Highly Uniform Resistive Switching Properties of Amorphous InGaZnO Thin Films Prepared by a Low Temperature Photochemical Solution Deposition Method. *ACS Appl. Mater. Interfaces* **2014**, *6*, 5012−5017.
(32) Schulman, A.; Lanosa, L. F.; Acha, C. Poole-Frenkel Effect and Variable-Range Hopping Conduction in Metal/YBCO Resistive Switching Devices. *J. Appl. Phys.* **2015**, *118*, 044511.
(33) Martinez, A.; Cho, B. J.; Kim, M. J. A Non-Invasive Approach to the Resistive Switching Physical Model of Ultra-Thin Organic-Inorganic Dielectric-Based ReRAMs. *Nanoscale* **2023**, *15*, 18794−18805.
(34) Hu, W.; Zou, L.; Lin, X.; Gao, C.; Guo, Y.; Bao, D. Unipolar Resistive Switching Effect and Mechanism of Solution-Processed Spinel Co_3O_4 Thin Films. *Mater. Des.* **2016**, *103*, 230−235.
(35) Hu, W.; Zou, L.; Chen, R.; Xie, W.; Chen, X.; Qin, N.; Li, S.; Yang, G.; Bao, D. Resistive Switching Properties and Physical Mechanism of Cobalt Ferrite Thin Films. *Appl. Phys. Lett.* **2014**, *104*, 143502.
(36) Ma, Y.; Goodwill, J. M.; Li, D.; Cullen, D. A.; Poplawsky, J. D.; More, K. L.; Bain, J. A.; Skowronski, M. Stable Metallic Enrichment in Conductive Filaments in TaO_x-Based Resistive Switches Arising from Competing Diffusive Fluxes. *Adv. Electron. Mater.* **2019**, *5*, 1800954.

https://doi.org/10.1021/acsomega.4c04429
ACS Omega 2024, 9, 33941−33948